

CoFFEE: Corrections For Formation Energy and Eigenvalues for charged defect simulations

Mit H. Naik, Manish Jain*

Centre for Condensed Matter Theory, Department of Physics, Indian Institute of Science, Bangalore 560012, India

Abstract

Charged point defects in materials are widely studied using Density Functional Theory (DFT) packages with periodic boundary conditions. The formation energy and defect level computed from these simulations need to be corrected to remove the contributions from the spurious long-range interaction between the defect and its periodic images. To this effect, the CoFFEE code implements the Freysoldt-Neugebauer-Van de Walle (FNV) correction scheme. The corrections can be applied to charged defects in a complete range of material shapes and size: bulk, slab (or two-dimensional), wires and nanoribbons. The code is written in Python and features MPI parallelization and optimizations using the Cython package for slow steps.

Keywords: Charged defects, Defect formation energy, Density Functional Theory, Eigenvalue corrections, electronic structure

PROGRAM SUMMARY

Program Title: CoFFEE

Program obtainable from: <http://www.physics.iisc.ernet.in/~mjain/pages/software.html>

Journal Reference:

Catalogue identifier:

Licensing provisions: Open source BSD License

Programming language: Python

Computer: Any computer with Python installed. The code has been tested with Python2.7 and Python3.6.

*Corresponding author.

E-mail address: mjain@physics.iisc.ernet.in

Preprint submitted to Computer Physics Communications

October 23, 2017

Operating system: Unix/Linux/Windows

RAM: 5-1000 MB (dependent on system size)

Keywords: Density Functional Theory, Defect formation energy, Charged defects, Eigenvalue corrections, Electronic Structure, GW

Classification: 7.1, 7.3

External routines/libraries: numpy, scipy, mpi4py, matplotlib

Nature of problem: Most electronic structure codes based on Density Functional Theory use periodic boundary conditions. This leads to spurious electrostatic interactions during simulation of charged defects, which affects the computed defect formation energy and the defect eigenvalue. *Solution method:* We implement the Freysoldt-Neugebauer-Van de Walle (FNV) correction scheme to correct the defect formation energy and eigenvalues. Our implementation can be applied to charged defects in 3D bulk materials as well as materials having 2D and 1D geometries.

Running time: 1-600 minutes (depends on the number of processors and system size)

1. Introduction

Point defects, ubiquitous in materials, influence their electrical and optical properties. First principles electronic structure calculations have proven to be vital in understanding and predicting the role of defects [1, 2, 3, 4, 5, 6, 7, 8, 9, 10, 11, 12, 13, 14, 15, 16, 17, 18]. Defect engineering to enhance or suppress certain characteristics of materials often rely on such simulations for inputs [19, 20, 21, 22, 23, 24, 25].

Intrinsic point defects in materials are generally found in low concentrations, about one in a million atoms in 3D solids to one in a thousand atoms in 2D materials. Simulations thus attempt to study isolated defects in materials. However, a large number of first principles calculation codes based on Density Functional Theory (DFT) employ periodic boundary conditions. As a result, in order to simulate and understand isolated defects, super cells are constructed. The size of the super cell is chosen to minimize the overlap of the defect wavefunction with its periodic image in neighboring cells [1, 26, 27, 28, 29, 30, 31]. The computed formation energy of non-shallow neutral defects in such calculations is found to converge quickly with the super cell size.

Charged point defects are simulated by artificially introducing a compensating uniform background charge to avoid the divergence in the electro-

static energy. The formation energy of charged defects show slow convergence with super cell size due to the Coulomb interaction between the defect charge and its periodic images. The super cell sizes necessary to completely overcome these spurious defect-defect interactions are computationally intractable. The defect energy levels in the gap are also affected similarly, and shows slow convergence with super cell size [27, 32, 33]. Furthermore, since the uniform background charge is artificially introduced, an absolute reference for the electrostatic potential is undefined. The potential in the defect supercell thus needs to be aligned with the bulk potential, in accordance with the chosen reference of the Fermi level with respect to the bulk VBM.

Several *a posteriori* correction schemes have been developed to tackle this issue [26, 28, 34, 35, 29, 36, 37]. Most of the correction schemes involve solving the Poisson equation for a model system, and aligning of potentials, to derive the correction to the formation energy. In particular, the scheme proposed by Freysoldt, Neugebauer and Van de Walle (FNV) has gained a lot of popularity owing to its consistency in deriving accurate corrections for charged defects in numerous materials [26]. This scheme has been extended to low-dimensional systems as well, and shown to perform well [38, 39, 40, 41, 42, 43, 44]. However, a generalized correction scheme implementation that works with bulk as well as low-dimensional systems is absent in the various DFT packages, or as an independent package [45, 46]. The recent independent packages are restricted to compute the corrections for charged defects in bulk systems alone [45, 46].

We present a complete electrostatic corrections package, CoFFEE: Corrections For Formation Energy and Eigenvalues for charged defect simulations. The package is applicable to charged defects in materials ranging bulk solids, interfaces, surfaces/slabs, two-dimensional (2D) materials, nanowires and nanoribbons. These materials can be classified according to the number of periodic directions, into 3D (bulk) , 2D (slabs, 2D materials) and 1D (nanowires, nanoribbons) systems. We implement a generalized Poisson solver based on the FNV correction scheme with a gaussian model charge distribution. Tools to compute the potential alignment terms in the FNV correction scheme are also provided with the package. The code is written entirely in Python [47]. We use Message Passing Interface (MPI) to parallelize the code and Cython [48] to accelerate slow steps. Our implementation can be used alongside any DFT package to obtain an *a posteriori* correction for the formation energy and the defect level position in the gap, for the charged defect being simulated.

2. Theoretical framework

The formation energy of a neutral defect in a material is given by:

$$E_0^f[\vec{R}_0](\epsilon_F) = E_0^{\text{tot}}[\vec{R}_0] - E_{\text{pristine}} - n_x \mu_x, \quad (1)$$

where ϵ_F is the Fermi level, $E_0^{\text{tot}}[\vec{R}_0]$ is the total energy of a system containing a neutral defect with atom positions at \vec{R}_0 . E_{pristine} represents the total energy of a pristine super cell of the same size. n_x refers to the number of atoms of type x added (positive) or removed (negative) from the pristine system, and μ_x is the atom's chemical potential [27]. The neutral defect formation energy needs no electrostatic correction term due to the absence of any long range electrostatic defect-defect interactions.

The formation energy of a defect in charge state q is given by [27]:

$$E_q^f[\vec{R}_q](\epsilon_F) = \{E_q^{\text{tot}}[\vec{R}_q] + E_q^{\text{corr}}\} - E_{\text{pristine}} + q\{\epsilon_{\text{vbm}}^{\text{pristine}} + \epsilon_F - \Delta V_{0/p}\} - n_x \mu_x \quad (2)$$

The first term on the right hand side is the total energy of a system containing a defect in charge state q with the requisite finite-size electrostatic correction E_q^{corr} (described below). The formation energy is now a function of the Fermi level in the system, ϵ_F , with respect to the pristine valence band maximum (VBM), $\epsilon_{\text{vbm}}^{\text{pristine}}$.

$$\Delta V_{0/p} = V_0|_{\text{far}} - V_p \quad (3)$$

is a potential alignment term found by comparing the electrostatic potentials from a pristine calculation and far from the defect in a neutral defect calculation.

2.1. FNV correction scheme

The electrostatic correction term, E_q^{corr} , is incorporated to correct the spurious interaction between the defect charge and its periodic images. In the FNV scheme, this term is given by [27, 26]:

$$E_q^{\text{corr}} = E_q^{\text{lat}} - q\Delta V_{q-0/m} \quad (4)$$

where $E_q^{\text{lat}} = E_q^{\text{iso,m}} - E_q^{\text{per,m}}$ is obtained from a model calculation. It involves solving the Poisson equation using a model charge distribution, $\rho^m(\mathbf{r})$, and

model dielectric profile under periodic boundary conditions to obtain the potential, $V_q^{\text{per,m}}(\mathbf{r})$ [27, 26]. $E_q^{\text{per,m}}$ is then given by:

$$E_q^{\text{per,m}} = \frac{1}{2} \int_{\Omega} \rho^m(\mathbf{r}) V_q^{\text{per,m}}(\mathbf{r}) d\mathbf{r} \quad (5)$$

where the integral is over the super cell volume, Ω . $E_q^{\text{per,m}}$ is evaluated for larger super cells and extrapolated to obtain $E_q^{\text{iso,m}}$. Performing larger super cell calculations within this model is computationally inexpensive compared to a DFT calculation on such systems. E_q^{lat} accounts for the long range interactions. The dependence of E_q^{corr} on the model charge distribution is eliminated by the second term in 4. $\Delta V_{q-0/m}$ is a potential alignment term found by comparing the model potential to the DFT difference potential:

$$\Delta V_{q-0/m} = (V_q^{\text{DFT}} - V_0^{\text{DFT}})|_{\text{far}} - V_q^{\text{per,m}}|_{\text{far}} \quad (6)$$

2.2. Model calculation

The model super cell calculation for $E_q^{\text{per,m}}$ involves solving the Poisson equation for the periodic model potential, $V_q^{\text{per,m}}(\mathbf{r})$ [39, 38, 42]:

$$\nabla \cdot [\varepsilon(\mathbf{r}) \nabla V_q^{\text{per,m}}(\mathbf{r})] = -4\pi \rho^m(\mathbf{r}) \quad (7)$$

where $\varepsilon(\mathbf{r})$ is the dielectric tensor profile of the material, $\rho^m(\mathbf{r})$ is the model charge distribution. The dielectric tensor can be obtained using Density Functional Perturbation Theory (DFPT) [49, 50]. Eqn 7 can be effectively solved in the reciprocal space [39, 38, 42]:

$$\sum_{\mathbf{G}'} \sum_{i=1}^3 G_i G'_i \varepsilon_{ii}(\mathbf{G} - \mathbf{G}') V_q^{\text{per,m}}(\mathbf{G}') = 4\pi \rho^m(\mathbf{G}) \quad (8)$$

where ε_{ii} are the diagonal terms of the dielectric tensor. $V_q^{\text{per,m}}(\mathbf{G}' = \mathbf{0})$ is set to zero, which is equivalent to introducing a uniform, neutralizing background charge. The number of \mathbf{G} vectors used in the calculation is determined by an energy cut off.

As one is interested in the long range corrections, ε in the material can be assumed to have no spatial profile; however, in general, it is a 3×3 tensor. In a 3D bulk system with an isotropic dielectric, $V_q^{\text{per,m}}$ can be obtained from Eqn 8 as:

$$V_q^{\text{per,m}}(\mathbf{G}) = \frac{4\pi \rho^m(\mathbf{G})}{\varepsilon |\mathbf{G}|^2} \quad (9)$$

For slab or two-dimensional systems, on the other hand, the dielectric tensor, while not having any profile inside the material, would still have a spatial profile in the aperiodic direction, say z [39, 38].

$$\begin{bmatrix} \varepsilon_{\parallel}^1(z) & 0.0 & 0.0 \\ 0.0 & \varepsilon_{\parallel}^2(z) & 0.0 \\ 0.0 & 0.0 & \varepsilon_{\perp}(z) \end{bmatrix}$$

where $\varepsilon_{\parallel}^1(z)$ and $\varepsilon_{\parallel}^2(z)$ is the dielectric profile for the in-plane dielectric constants \vec{a}_1 and \vec{a}_2 and $\varepsilon_{\perp}(z)$ is the dielectric profile for the out-of-plane dielectric constant of the material.

For slab systems or a 2D material with more than one atom thickness, like transition metal dichalcogenides, phosphorene, etc., the dielectric profile used is of the form, [39, 38]:

$$\varepsilon(z) = \frac{1}{2}(\varepsilon^v - \varepsilon^m)\text{erf}\left(\frac{z - t_1}{s}\right) - \frac{1}{2}(\varepsilon^v - \varepsilon^m)\text{erf}\left(\frac{z - t_2}{s}\right) + \varepsilon^v \quad (10)$$

where t_1 and t_2 are the edges of the slab in the z -direction in the simulation cell. A parameter, s , is used with the error function (erf) to smoothen the profile at the slab edges. ε^m is the dielectric constant of the material, found using DFPT [39]. ε^v is the dielectric constant of the space surrounding the material, set to 1 for vacuum. A sample slab profile is shown in Fig 1 (a). For a 2D material with one atom thickness, like Boron Nitride (BN), Silicon Carbide (SiC), graphene, etc., the dielectric profile used is a gaussian to mimic the planar-averaged charge density of the material in the z -direction. A sample profile is shown in Fig 1 (b).

For slab or 2D systems, Eqn 8 can then be written as:

$$\begin{aligned} & \sum_{G'_z} [\varepsilon_{\perp}(G_z - G'_z)] G'_z G_z V_q^{\text{per,m}}(G_x, G_y, G'_z) \\ & + \sum_{G'_z} [\varepsilon_{\parallel}(G_z - G'_z)] (G_x^2 + G_y^2) V_q^{\text{per,m}}(G_x, G_y, G'_z) = 4\pi\rho^m(G_x, G_y, G_z) \quad (11) \end{aligned}$$

The average potential, $V_q^{\text{per,m}}(\mathbf{G} = 0)$, is set to zero, to introduce a neutralizing background charge.

For a quasi-1D system like nanowires or nanoribbons, with periodicity along the z direction, the dielectric tensor profile is of the form [42] :

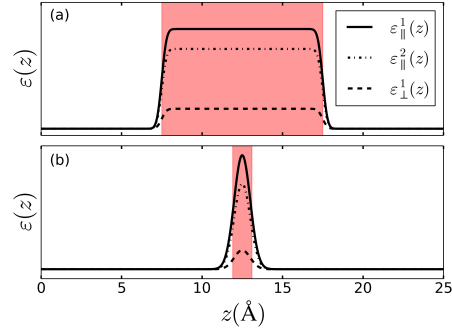


Figure 1: (Color online) (a) Sample profile for slab systems or 2D materials with more than one atom thickness. (b) Sample profile for single atom thickness 2D materials.

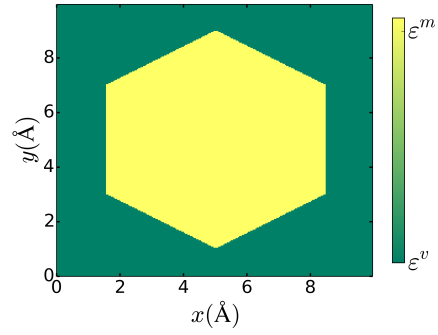


Figure 2: (Color online) Sample profile for a nanowire along z direction with a hexagonal cross-section. ϵ^m is the dielectric constant of the material and ϵ^v that of the environment ($\epsilon^v = 1$ for vacuum).

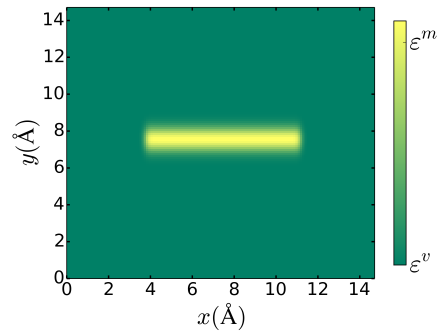


Figure 3: (Color online) Sample profile for a nanoribbon with periodicity along the z direction. ϵ^m is the dielectric constant of the material and ϵ^v that of the environment ($\epsilon^v = 1$ for vacuum).

$$\begin{bmatrix} \varepsilon_{\perp}(x, y) & 0.0 & 0.0 \\ 0.0 & \varepsilon_{\perp}(x, y) & 0.0 \\ 0.0 & 0.0 & \varepsilon_{\parallel}(x, y) \end{bmatrix}$$

where $\varepsilon_{\perp}(x, y)$ is the profile for the dielectric constant perpendicular to the wire and $\varepsilon_{\parallel}(x, y)$ is the profile for the dielectric constant along the wire. A sample profile for a silicon nanowire along the [111] direction is shown in Fig. 2. The wire, oriented along the z direction, has a hexagonal cross-section [42]. The profile is constructed such that the points inside the wire have the dielectric constant of the material, ε^m , and the points outside have ε^v . A sample profile for a BN nanoribbon is shown in Fig. 3. The profile is constructed to mimic the electron charge density of the material by combining a slab like profile (Eqn 10) along the width of the nanoribbon and a gaussian along the out-of-plane direction. Eqn 8, for 1D systems, can then be written as [42]:

$$\begin{aligned} \sum_{G'_x, G'_y} [\varepsilon_{\parallel}(G_x - G'_x, G_y - G'_y) G_z^2 \\ + \varepsilon_{\perp}(G_x - G'_x, G_y - G'_y)(G_x G'_x + G_y G'_y)] V(G'_x, G'_y, G_z) \\ = 4\pi\rho(G_x, G_y, G_z) \end{aligned} \quad (12)$$

We set $V(\mathbf{G} = 0) = 0$ here, to introduce a neutralizing background charge.

2.3. Defect eigenvalue correction

The defect eigenvalues, like the formation energy, show slow convergence with the super cell size [32, 33]. The correction to the eigenvalue is given by [33]:

$$\epsilon_q^{\text{corr}} = \frac{-2}{q} E_q^{\text{corr}} \quad (13)$$

where E_q^{corr} is the FNV correction term, Eqn 4. The correction is negative for positively charged defects and positive for negatively charged defects. Defect level corrections are crucial in studying defects using the DFT+GW formalism [32, 33, 2, 3, 1] and also in interpreting absorption experiments.

3. Test Systems

We show the performance of our code in correcting the formation energies and defect levels in the following systems:

1. Bulk: Carbon vacancy in diamond in charge state -2, V_C^{-2} .
2. 2D: Sulfur vacancy in monolayer MoS₂ in charge state -1, V_S^{-1} .
3. 1D: Boron vacancy in BN nanoribbon in charge state -1, V_B^{-1} .

All the DFT calculations are performed using the plane-wave, pseudopotential package, Quantum Espresso [51]. We perform simulations on a range of super cell sizes and compare the extrapolated formation energy and defect level (to the isolated limit) with the corrected formation energy and defect level.

3.1. Vacancy in diamond, V_C^{-2}

We perform DFT calculations on different cubic super cell sizes with number of C atoms ranging from 64 to 1024. We use norm-conserving pseudopotentials and the LDA exchange correlation functional [52]. The wavefunctions are expanded in plane-waves upto an energy cut off of 60 Ry. For the 64 atom, $2 \times 2 \times 2$ super cell, a k-point sampling of $5 \times 5 \times 5$ was used. An equivalent sampling is used for the other super cell sizes. We did not include any atomic relaxations.

The model calculation is performed using the CoFFEE code, solving Eqn 9. The defect is modelled with a gaussian of width 2.6 bohr, a dielectric constant of 5.76 and a plane wave energy cut off of 16 Ry. Fig. 4 (a) shows the defect wavefunction charge density, $|\psi_d|^2$, and the model charge density. For bulk systems, it is not necessary that the width of the Gaussian model charge match the defect wavefunction charge density. It suffices if the width is appropriately small to keep the model charge inside the cell. Note also that the plane wave energy cut off required to converge the model calculation is inversely proportional to the width of the Gaussian. Fig. 4 (c) shows the extrapolation of the model energy, $E_{-2}^{\text{per,m}}$ (Eqn 5), with super cell size, Ω . The energy is fit with a polynomial of the form:

$$p(\Omega) = f_1 + f_2/\Omega^{1/3} + f_3/\Omega \quad (14)$$

f_1 here corresponds to the isolated model energy, $E_{-2}^{\text{iso,m}}$. The fitting parameters here are: $f_1 = 2.04$, $f_2 = -14.19$ and $f_3 = 120.85$. The lattice correction is then given by: $E_{-2}^{\text{iso,m}} - E_{-2}^{\text{per,m}}$ (Eqn 4). Fig. 4 (b) compares the planar averaged model potential and the DFT difference potential which contribute to the potential alignment term, $\Delta V_{q=0/m}$ (Eqn 6) for a $3 \times 3 \times 3$ super cell. The defect in this calculation is at the center of the cell. The model potential matches well with the DFT difference potential far from the defect, leading

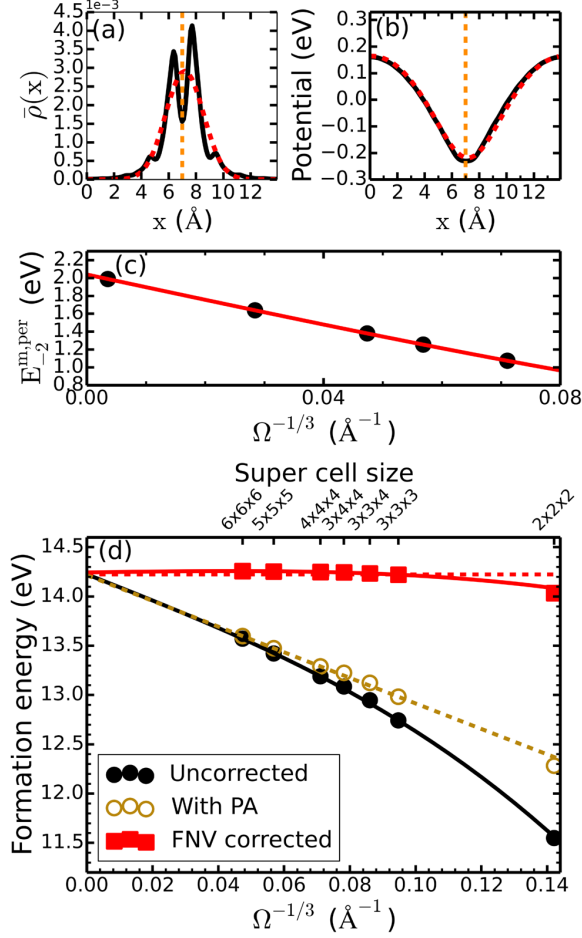


Figure 4: (Color online) (a) Black solid line refers to the planar averaged defect wavefunction charge density. Red dashed line refers to the planar averaged model charge density. (b) Black solid line refers to the planar averaged DFT difference potential, $V_q^{\text{DFT}} - V_0^{\text{DFT}}$, in 6 from a $3 \times 3 \times 3$ super cell. Red dashed line refers to the planar averaged model potential for the same size super cell. (c) Scaling of the total energy from the model calculation with super cell volume, Ω . (d) Black solid line shows the fit to the scaling of the uncorrected formation energy (filled black dots) with super cell size. The unfilled golden circles show the formation energy with only potential alignment corrections. The red squares show the FNV corrected formation energy for various super cell sizes. The red solid line is a fit to the FNV corrected formation energies and the horizontal red dashed line marks the extrapolated value of the uncorrected formation energies.

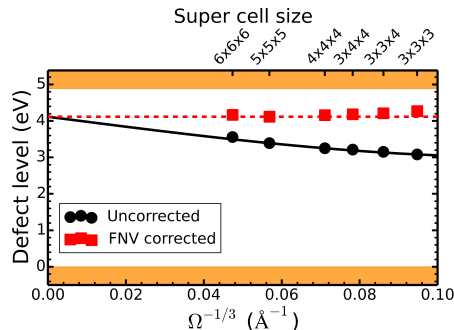


Figure 5: (Color online) Black solid line shows the fit to the scaling of the uncorrected defect eigenvalue (filled black dots) with super cell size. The horizontal red dashed line marks the extrapolated value of the uncorrected defect level. The red squares show the FNV corrected defect eigenvalue.

to a very small correction. On the other hand, the potential alignment term, $\Delta V_{0/p}$ in Eqn 2, which compares the potential far from the neutral defect to the pristine, has a substantial contribution.

The uncorrected formation energy of V_C^{-2} for various supercell sizes is fit using Eqn 14 to extrapolate to the isolated limit as shown in Fig. 4 (d). The chemical potential of carbon is taken from bulk diamond. The FNV corrected formation energy shows good agreement with the extrapolated value for super cell sizes larger than $2 \times 2 \times 2$. The correction scheme performs well when the defect wavefunction is localized well within the super cell; this is not the case with the $2 \times 2 \times 2$ super cell. The defect level accommodating the -2 charge is shown in Fig. 5 with respect to the pristine VBM eigenvalue in the charged super cell. It shows a similar scaling with super cell size and is corrected using Eqn 13.

3.2. Vacancy in monolayer MoS_2 , V_S^{-1}

We study sulfur vacancies in monolayer MoS_2 to demonstrate the electrostatic corrections in 2D or slab systems. The DFT calculations are performed using PAW pseudopotentials [53], PBE scheme for the exchange correlation functional [54]. A wavefunction cut off of 50 Ry, and charge density cut off of 500 Ry is used. We perform calculations on four super cell sizes: $\alpha \times \alpha \times \alpha$, for $\alpha = 4, 5, 6$ and 8. The α refers to the scaling of the cell dimension. It has been reported that scaling just the in-plane supercell, keeping the amount of vacuum fixed, leads to a divergence in the model energy [38]. We hence uni-

formly scale the vacuum with the in-plane super cell. For $\alpha = 6$, the vacuum thickness is $\sim 16\text{\AA}$ and thickness of MoS_2 is 3.2\AA . The k-point sampling for these is chosen to effectively sample the unit cell Brillouin zone with a grid better than $12 \times 12 \times 1$. The atoms are relaxed to their equilibrium positions such that the force on each atom is $\leq 10^{-2}$ eV/ \AA .

The model calculation is performed solving Eqn 11. The dielectric profile is chosen as in Eqn 10, with $\varepsilon_m = 15$ in the direction parallel to the material and $\varepsilon_m = 2$ in the perpendicular direction. The smoothening parameter, s , is chosen to be 0.38 bohr. The dielectric constants are determined using DFPT as prescribed in reference [39]. The plane wave energy cut off is set to 30.0 Ryd. The defect is modelled with a Gaussian of width 1.9 bohr as shown in Fig. 6 (a). It is important here to choose a Gaussian width that mimics the defect charge density. Choosing a width too large that spills beyond the gray shaded region in Fig. 6 (a) would affect the results. The defect wavefunction charge density can be fit to a Gaussian using the script *g-fit.py* supplied with the CoFFEE code.

Fig 6 (b) compares the planar averaged model potential with the planar averaged DFT difference potential, $V_{-1}^{\text{DFT}} - V_0^{\text{DFT}}$, for the $\alpha = 6$ supercell. The DFT difference potential used here is from unrelaxed calculations and shows good agreement with the model potential far from the defect. Fig 6 (c) shows the variation of the model electrostatic energy with two different scalings of the super cell size: $\alpha \times \alpha \times \alpha$ and $\alpha \times \alpha \times 1.6\alpha$. For $\alpha \times \alpha \times 1.6\alpha$ super cell scaling, the vacuum thickness is 1.6 times larger than that of $\alpha \times \alpha \times \alpha$ scaling. The interaction between the periodic charges is unscreened in the out-of-plane direction, and screened by the material in the in-plane direction. The model energy is thus strongly dependent on the vacuum thickness, for small super cell sizes. As expected, at the infinite limit ($\alpha = \infty$), the two scalings extrapolate to the same value. The model scaling plots clearly do not follow a simple fit as in the case of bulk solids due to the spatially varying dielectric profile. The energy is fit with a polynomial of degree five in α^{-1} : $E_{-1}^{\text{per,m}}(\alpha) = f_0 + f_1\alpha^{-1} + f_2\alpha^{-2} + f_3\alpha^{-3} + f_4\alpha^{-4} + f_5\alpha^{-5}$ [39]. The isolated model energy is given by $f_0 = E_{-1}^{\text{iso,m}}$, and the lattice correction is given by: $E_{-1}^{\text{iso,m}} - E_{-1}^{\text{per,m}}$. The fitting parameters, for $\alpha \times \alpha \times \alpha$ scaling, are found to be: $f_0 = 0.66$, $f_1 = -4.04$, $f_2 = 54.95$, $f_3 = -388.69$, $f_4 = 1267.38$ and $f_5 = -1579.27$.

Fig 7 (a) shows the scaling of the uncorrected formation energy of neutral S vacancy, V_S^0 , and -1 charged S vacancy, V_S^{-1} , as a function of super cell

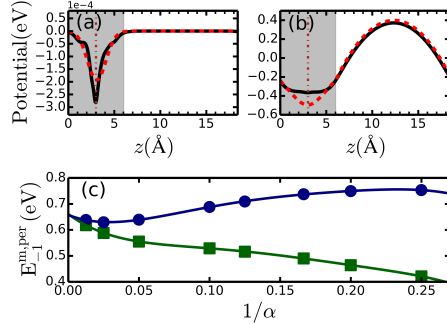


Figure 6: (Color online) (a) Black solid line shows the planar averaged defect wavefunction charge density, along the out-of-plane direction, for the $\alpha = 6$ super cell of MoS₂. The red dashed line shows the planar averaged Gaussian model charge. The shaded gray region marks the location and width of the dielectric profile (Eqn. 10). (b) Black solid line shows the planar averaged DFT difference potential: $V_{-1}^{\text{DFT}} - V_0^{\text{DFT}}$, along the out-of-plane direction for the same cell. The red dashed line shows the planar averaged model potential. The vertical brown dot-dashed line marks the center of the Gaussian model charge. (c) Total energy from the model calculation with two super cell size scalings: $\alpha \times \alpha \times \alpha$ (green squares) and $\alpha \times \alpha \times 1.6\alpha$ (blue circles).

size. The chemical potential of sulfur is taken from the cyclo-S₈ allotrope of sulfur. The neutral vacancy formation energy is well converged and shows no scaling with system size. The scaling of the charged vacancy formation energy is fit with a polynomial of the form [39]: $E_{-1}^f(\alpha) = t_0 + (f_1\alpha^{-1} + f_2\alpha^{-2} + f_3\alpha^{-3} + f_4\alpha^{-4} + f_5\alpha^{-5}) + t_3\alpha^{-3}$. The additional terms are necessary to capture the scaling of the potential alignment term with system size. t_0 and t_3 are found to be 4.71 and -8.69 respectively. The FNV corrected formation energy shows excellent agreement with the extrapolated value for all the super cell sizes considered. Fig 7 (b) shows the dependence of the defect level accommodating the -1 charge with system size. The uncorrected values are fit with a polynomial of the form: $\epsilon_{-1}(\alpha) = t_0 + 2 \times (f_1\alpha^{-1} + f_2\alpha^{-2} + f_3\alpha^{-3} + f_4\alpha^{-4} + f_5\alpha^{-5}) + t_3\alpha^{-3}$. The corrected eigenvalues are in good agreement with the extrapolated value.

3.3. Vacancy in BN nanoribbon, V_B^{-1}

To show the application of the code for 1D systems, we study B vacancy in a BN nanoribbon of thickness 13.39 Å [13]. We perform calculations on three super cell sizes: α ($1 \times 2.31 \times 1$), for $\alpha = 6, 8, 10$. For $\alpha = 6$, the simulation cell dimensions are 15 Å, 35 Å and 15 Å, in the x , y and z directions respectively.

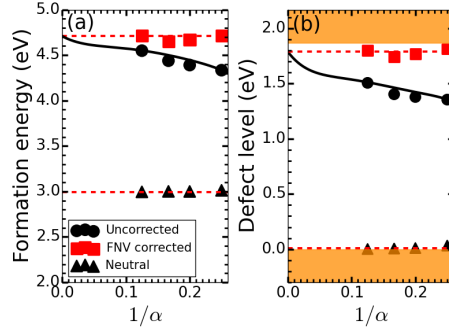


Figure 7: (Color online) (a) Black solid line shows the fit to the scaling of the uncorrected formation energy (filled black dots) of V_S^{-1} . The red squares show the FNV corrected formation energy, the horizontal red dashed line shows the extrapolated value from the uncorrected formation energies. The triangles show the formation energy of the neutral defect. (b) Black solid line shows the fit to the uncorrected defect level (filled black dots) holding the added electron in V_S^{-1} . The red squares show the FNV corrected defect level. The horizontal red dashed line shows the extrapolated value from the uncorrected levels. The triangles show the position of the filled defect level in V_S^0 . The orange bands mark the valence and conduction band edges, the VBM is set to zero.

The z direction is the periodic direction. A vacuum of 15\AA and 22\AA has been introduced in the out-of-plane x direction and lateral y direction. The thickness of the ribbon is fixed in these cell sizes, with the number of atoms in the periodic direction and the vacuum padding scaling with α . The ribbon is passivated on either side with H atoms. Ribbon in $\alpha = 6$ super cell with a B vacancy is shown in Fig 8 (a). The DFT calculations are performed using norm conserving pseudopotentials and the PBE scheme is used for the exchange correlation functional [54]. A plane wave energy cut off of 70 Ry is used for the wavefunctions. The Brillouin zone is sampled with a $1 \times 1 \times 2$ grid for $\alpha = 6, 8$ and with the Γ point for $\alpha = 10$. We relaxed the atoms in the super cell containing the defect until the force on each atom is $\leq 10^{-2}$ eV/ \AA .

For the model calculation, we use a dielectric profile as shown in Fig 3. A slab like profile, similar to the one used for MoS_2 , is used along the width of the nanoribbon and a gaussian profile in the out-of-plane, x direction. The width of the slab is taken to be that of the width of the nanoribbon, with a smoothing parameter of 0.37 bohr. The gaussian width is taken to be 0.86 bohr, chosen to mimic the electron charge density in that direction. ϵ^m used is 2.9 along the x direction and 12 along the other two directions. These

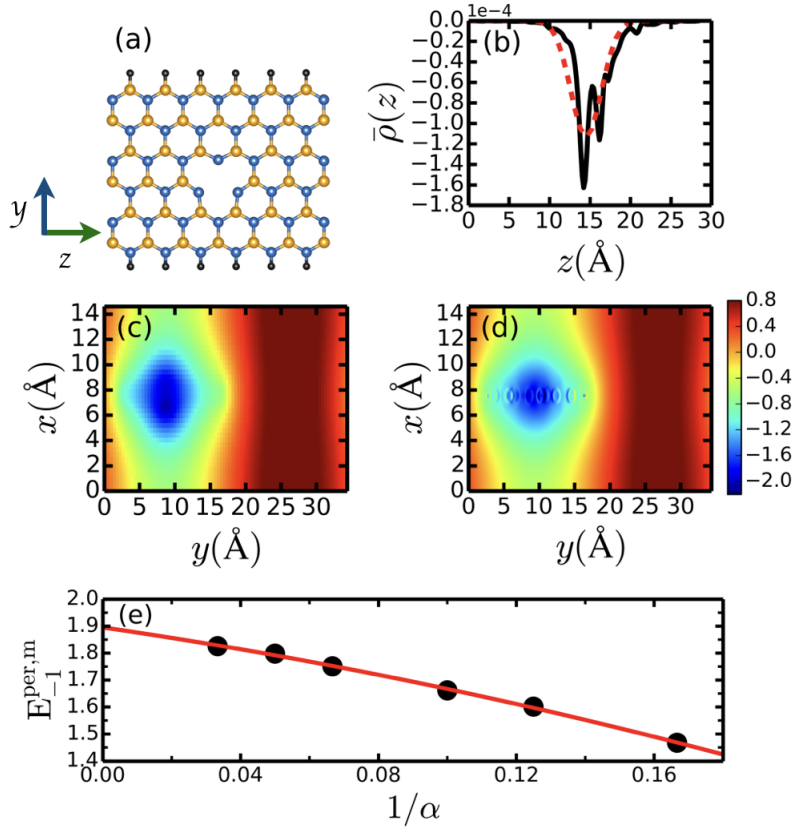


Figure 8: (Color online) (a) B vacancy in the $6 \times 19 \times 6$ BN nanoribbon super cell. The yellow spheres denote the B atoms, blue spheres the N atoms and black spheres the H atoms. (b) Black solid line refers to the planar averaged defect wavefunction charge density, plotted along the z direction. The red dashed lines refers to the planar averaged model Gaussian charge density. (b) scaling of the energy from the model calculation for V_B^{-1} with super cell size, α ($1 \times 2.31 \times 1$). (c) z -averaged model potential for the $6 \times 19 \times 6$ cell. (d) z -averaged DFT difference potential: $V_{-1}^{\text{DFT}} - V_0^{\text{DFT}}$ for the $6 \times 19 \times 6$ cell.

are computed from DFPT calculations on a monolayer BN sheet. We use a gaussian model charge with width 1.89 bohr and integrated charge -1. The planar averaged model charge and the defect wavefunction charge density are shown in Fig. 8 (b). The calculation is performed with a plane wave energy cut off of 16.0 Ry. Fig 8 (e) shows the scaling of the computed $E_{-1}^{\text{per,m}}$ as a function of $1/\alpha$. The points are fit with a third degree polynomial in α^{-1} : $E_{-1}^{\text{per,m}}(\alpha) = f_0 + f_1\alpha^{-1} + f_2\alpha^{-2} + f_3\alpha^{-3}$. f_0 then corresponds to the isolated model energy, $E_{-1}^{\text{iso,m}}$, and the lattice correction is given by: $E_{-1}^{\text{iso,m}} - E_{-1}^{\text{per,m}}$. The fitting parameters are found to be: $f_0 = 1.90$, $f_1 = -1.85$, $f_2 = -4.35$ and $f_3 = 0.58$. The potential alignment terms, $\Delta V_{q=0/m}$ and $\Delta V_{0/p}$, are calculated by comparing the potentials in the out-of-plane, x direction, far from the defect. Both these terms are found to be small (< 20 meV). Fig 8 (c) and (d) show the DFT difference potential in Eqn 6 and the model potential, respectively, for $\alpha = 6$ super cell size. The defect is at $(x, y) = (7.5, 9)$ in the figure. The model potential matches well with the DFT difference potential far from the defect.

Fig 9 (a) shows the scaling of the uncorrected formation energy of neutral vacancy, V_B^0 , and -1 charged vacancy, V_B^{-1} , as a function of $1/\alpha$. The formation energy is computed for nitrogen-rich conditions. The chemical potential for N is taken from N_2 molecule. Formation energy of the neutral vacancy is well converged and shows no scaling with the system size. The uncorrected formation energy of the charged vacancy is fit with a polynomial of the form: $E_{-1}^f(\alpha) = t_0 + (f_1\alpha^{-1} + f_2\alpha^{-2} + f_3\alpha^{-3}) + t_3\alpha^{-3}$. t_0 and t_3 are found to be 9.39, -3.92. The FNV corrected formation energy shows excellent agreement with the extrapolated value for all the super cell sizes considered. Fig 9 (b) shows the dependence of the defect level accomodating the -1 charge with system size. The uncorrected values are fit with a polynomial of the form: $\epsilon_{-1}(\alpha) = t_0 + 2 \times (f_1\alpha^{-1} + f_2\alpha^{-2} + f_3\alpha^{-3}) + t_3\alpha^{-3}$. The corrected eigenvalues are in good agreement with the extrapolated value.

4. Workflow

The general steps involved in computing corrections for the formation energy of a charged defect are the following (Fig. 10):

1. Compute the total energy of the pristine super cell of the same size. Save the DFT potential in cube/xsf format.

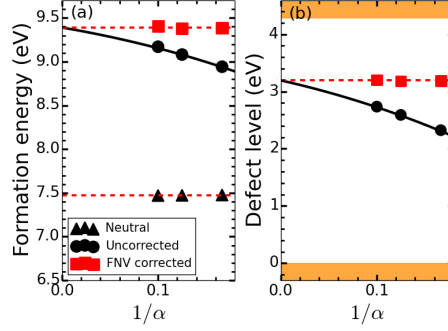


Figure 9: (Color online) (a) Black solid line shows the fit to the scaling of the uncorrected formation energy of -1 charged B vacancy in BN nanoribbon (filled black dots) with super cell size. The red squares show the FNV corrected formation energy. The horizontal red dashed line shows the extrapolated value from the uncorrected formation energies. The triangles show the formation energy of the neutral defect. (b) Filled black dots show the uncorrected defect eigenvalue in the gap as a function of system size. Black solid line is the fit to these, and the isolated limit extrapolation is marked with the red dashed line. The red squares mark the FNV corrected eigenvalues. The orange bands mark the valence and conduction band edges, the VBM is set to zero.

2. Compute the total energy of the super cell (say $n \times n \times n$) containing the neutral defect. Save the DFT potential in cube/xsf format.
3. Compute the total energy of the super cell containing the charged defect. Save the DFT potential in cube/xsf format.
4. Compute E_q^{lat} term: Compute the model energy for various super cell sizes and extrapolate to obtain $E_q^{\text{iso,m}}$. E_q^{lat} is then given by: $E_q^{\text{iso,m}} - E_q^{\text{per,m}}$ ($n \times n \times n$).
5. Compute the potential alignment term $\Delta V_{0/p}$, Eqn. 3. The utility script *dV_0p.py* can be used to compute this.
6. Compute the potential alignment term $\Delta V_{q-0/m}$, Eqn. 6. The utility *dV_mD.py* can be used to compute this.

The first three steps are performed by the user with the DFT electronic structure code of his/her choice. The xsf/cube file formats are commonly used to visualize data. Most electronic structure codes provide utilities to convert the DFT potential after a self consistent calculation into these formats. These formats act as an interface between the DFT calculation and the CoFFEE code. The CoFFEE code aids in computing steps 4, 5 and 6. The model calculations are performed by solving the Poisson equation, as

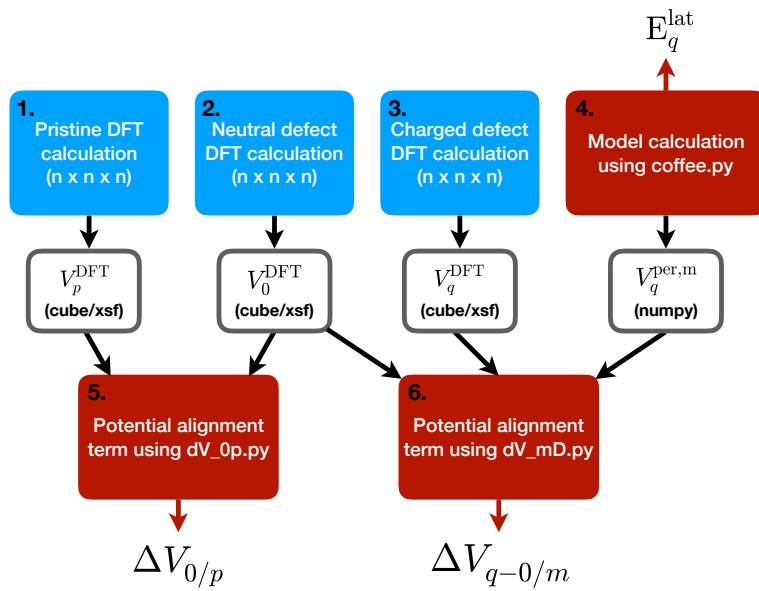


Figure 10: (Color online) The workflow involved in computing the formation energy of a charged defect. The blue boxes are performed using a DFT electronic structure code. CoFFEE aids in computing the corrections, the red boxes. ($n \times n \times n$) refers to the super cell size.

detailed above. Details on preparing the input file and running the CoFFEE code to perform these calculations are provided to some extent in the next section and exhaustively in the user guide of the code. The user guide is available for download with the distribution.

5. CoFFEE code framework

5.1. Layout

On unzipping the tar file after download, the CoFFEE folder contains the following directories: *PoissonSolver*, *PotentialAlignment* and *Examples*, and a script *coffee.py*. The script *coffee.py* is the main executable. It can be called from the user's working directory and it performs the model calculation by sequentially calling the relevant functions as depicted in Fig 11. The script *coffee.py* reads input from a file. The input file contains parameters pertaining to the dimensions of the super cell, the dielectric profile and the model Gaussian charge. The next subsection describes the input file parameters. On running the script, the model total energy is printed out. The model potential, dielectric profile and model charge distribution are written as numpy save files on providing the appropriate flags in the input. The script is run for different supercell sizes and the model energy extrapolated as shown in Fig. 4 (c), 6 (c) and 8 (e) to obtain the isolated model energy.

The *PoissonSolver* folder holds *classes.py* which defines three classes: *cell*, *diel_profile* and *gaussian*. Each class has a function to read the parameters pertaining to it from the input file. The *cell* class has information regarding the cell parameters and the plane wave cut off to be used in the calculation. The *diel_profile* class has attributes regarding the dielectric profile to be used and functions to construct and Fourier transform the requisite profile. The *gaussian* class has attributes regarding the construction and Fourier transform of the model gaussian charge. The *PoissonSolver* folder also consists of three routines, *Solver.py*, *construct_eps.py* and *PS_main.py*. *construct_eps.py* is used to select and construct the appropriate dielectric profile, based on the user input. *Solver.py* is used to select the poisson solver to be run. *PS_main.py* contains the solvers for 1D (*PS_1D*), 2D (*PS_2D*) and bulk (*PS_3D*) systems.

5.2. Input file

The input file is divided into three sections designated with "&CELL_PARAMETERS", "&DIELECTRIC_PARAMETERS" and "&GAUSSIAN_PARAMETERS". Each

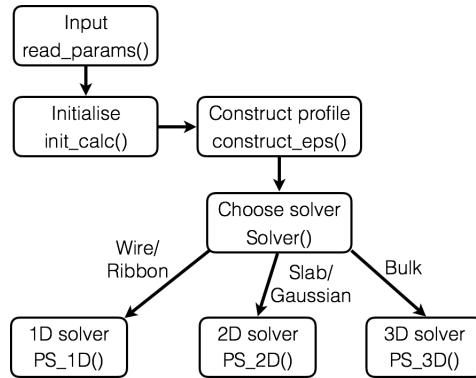


Figure 11: Program flow of the script *coffee.py* to compute the total energy from a model calculation using the CoFFEE code.

section is ended with a `"/` and contains, in the intervening space, the parameters relevant to the respective section. The following is an example of an input file for V_C^{-2} in diamond.

```

&CELL_PARAMETERS
# Normalized lattice vectors: a1, a2 and a3
Lattice_Vectors(normalized):
1.000000000  0.000000000  0.000000000
0.000000000  1.000000000  0.000000000
0.000000000  0.000000000  1.000000000

# Cell dimensions. Provide "angstrom" in place
# of "bohr" if you wish to specify
# these values in angstrom units.
# These are multiplied to a1, a2 and a3 respectively.
Cell_dimensions bohr
26.594331775231996 26.594331775231996 26.594331775231996

# G-vectors will be used upto this kinetic energy cut off.
# Provide "Rydberg" in place of "Hartree"
# if you wish to specify the cut off in Rydberg
# atomic units.
Ecut=20.0 Hartree
/
  
```

```

# Set "Bulk" here for 3D, bulk systems.
&DIELECTRIC_PARAMETERS Bulk
# Sets the value of the dielectric constant along a1, a2, a3.
Epsilon1_a1 = 5.76
Epsilon1_a2 = 5.76
Epsilon1_a3 = 5.76
/

&GAUSSIAN_PARAMETERS:
# The charge state of the defect being simulated.
Total_charge = -2

# The width of the model Gaussian charge being used.
# (default: bohr units)
Sigma = 2.614

# These set the center of the Gaussian in crystal
# units.
Centre_a1 = 0.5
Centre_a2 = 0.5
Centre_a3 = 0.5
/

```

The default unit of length is bohr, unless "angstrom" is explicitly specified after the number. Ecut stands for the plane wave energy cut off used in solving the Poisson equation. The string after &DIELECTRIC_PARAMETERS determines the dielectric profile and which Poisson solver is to be called. The dielectric parameters are provided in the input file along the crystal axes. The center of the model charge is specified in crystal units in the &GAUSSIAN_PARAMETERS, along with the charge it carries and the gaussian width. For the nanowire profile, the user can provide a list of points that form the boundary of the cross-section of the wire in a file, based on which the profile is created. The user guide lists all the possible input parameters and the properties they control. Also, the *Examples* folder has sample profiles for different materials.

5.3. Potential alignment

The *PotentialAlignment* directory holds two scripts: *dV_0p.py* and *dV_mD.py* to compute the two potential alignment terms, $\Delta V_{0/p}$ and $\Delta V_{q-0/m}$ in Eqn.

2 and 4. These scripts read the DFT potential from "cube" or "xsf" formats. *dV_0p.py* plots the planar averaged $V_0 - V_p$, in the desired direction. The difference far from the defect can then be read from the plot. This script reads input from a file. The format of the input file:

```
&dV_0p
file_type = cube # No quotes. Takes cube/xsf
file_neutral = n.cube # No quotes. Path to the neutral DFT potential file
file_pristine = p.cube # No quotes. Path to the pristine DFT potential file
plt_dir = a1 # No quotes. Takes a1/a2/a3. If a1
            # is specified, the data is averaged along a2
            # and a3 directions and the planar averaged data is plotted
            # along a1 in a file pa_dv0p_a1.plot
factor = Ryd # factor to be multiplied to the cube/xsf data. If the data is in
            # rydberg and the plot is needed in eV, specify
            # factor = Ryd. If the data is in Hartree units,
            # specify factor = Hartree
/
```

dV_mD.py plots the planar averaged ($V_q^{\text{DFT}} - V_0^{\text{DFT}}$) and $V_q^{\text{per,m}}|_{\text{far}}$ along the desired direction. These can be plotted as shown in Fig. 4 b, 6 b. This script reads input from a file. The format of the input file:

```
&dV_mD
file_type = cube # No quotes. Format of the DFT potential files: cube/xsf
file_model = m.npy # No quotes. Path to the model potential file (.npy)
file_charged = q.cube # No quotes. Path to the charged DFT potential file
file_neutral = n.cube # No quotes. Path to the neutral DFT potential file
plt_dir = a1 # No quotes. Takes a1/a2/a3. If a1
            # is specified, the data is averaged along a2
            # and a3 directions and the planar averaged data is plotted
            # along a1 in files DFTdiff_a1.plot, model_a1.plot
factor = Ryd # factor to be multiplied to the cube/xsf data. If the data is in
            # rydberg and the plot is needed in eV, specify
            # factor = Ryd. If the data is in Hartree units,
            # specify factor = Hartree
/
```

5.4. Solver parallelization and optimization

PS_1D, *PS_2D* and *PS_3D* are the poisson solver functions in *PS_main.py* for 1D, 2D and bulk systems. We do not use any parallelization for bulk systems, where the potential is obtained using Eqn 9, since the computation time is fairly small. We have, however, optimized this function with the help of Cython [48]. For 2D systems, linear equations of the form in Eqn 11 are solved. The number of reciprocal lattice vectors depends on the plane wave energy cut off set for the calculation. For N_{G_1} and N_{G_2} reciprocal lattice vectors along the in-plane reciprocal lattice directions, a set of $N_{G_1} \times N_{G_2}$ linear equations are solved. We use the iterative solver *bicgstab()* which is a part of the SciPy linear algebra package to solve these linear equations. These calculations are computationally intensive for large system sizes. We parallelize the total number of linear equations so that each process solves $N_{G_2} \times N_{G_1}/N_p$ equations, where N_p is the number of processes. The parallelization is done via MPI, using the package *mpi4py* [55]. For 1D systems, N_{G_z} linear equations are solved as shown in Eqn 14. These are again parallelized in the package in a similar manner. Furthermore, the efficiency of the *bicgstab()* routine is primarily determined by the time taken to compute matrix vector products. We optimized these products using Cython [48] to reduce the computation time.

6. Conclusion

We present a complete package, CoFFEE, for electrostatic corrections in charged defect simulations. We demonstrate the application of this code on three test systems, namely: bulk diamond, 2D MoS₂ and 1D BN nanoribbon. The corrected formation energy and defect eigenvalues for these systems are found to be in good agreement with the isolated limit extrapolation of the corresponding uncorrected quantities. The code, written completely in Python [47], is parallelized using MPI and the slowest steps accelerated using Cython [48].

7. Acknowledgments

We thank the Supercomputer Education and Research Centre (SERC) at IISc for providing the computational facilities.

References

References

- [1] C. Freysoldt, B. Grabowski, T. Hickel, J. Neugebauer, G. Kresse, A. Janotti, C. G. Van de Walle, First-principles calculations for point defects in solids, *Rev. Mod. Phys.* 86 (2014) 253–305. doi:10.1103/RevModPhys.86.253. URL <http://link.aps.org/doi/10.1103/RevModPhys.86.253>
- [2] A. Malashevich, M. Jain, S. G. Louie, First-principles DFT + *gw* study of oxygen vacancies in rutile TiO_2 , *Phys. Rev. B* 89 (2014) 075205. doi:10.1103/PhysRevB.89.075205. URL <http://link.aps.org/doi/10.1103/PhysRevB.89.075205>
- [3] M. Jain, J. R. Chelikowsky, S. G. Louie, Quasiparticle excitations and charge transition levels of oxygen vacancies in hafnia, *Phys. Rev. Lett.* 107 (2011) 216803. doi:10.1103/PhysRevLett.107.216803. URL <http://link.aps.org/doi/10.1103/PhysRevLett.107.216803>
- [4] S. Choi, M. Jain, S. G. Louie, Mechanism for optical initialization of spin in nv^- center in diamond, *Phys. Rev. B* 86 (2012) 041202. doi:10.1103/PhysRevB.86.041202. URL <http://link.aps.org/doi/10.1103/PhysRevB.86.041202>
- [5] L. Bjaalie, A. Janotti, K. Krishnaswamy, C. G. Van de Walle, Point defects, impurities, and small hole polarons in GdTiO_3 , *Phys. Rev. B* 93 (2016) 115316. doi:10.1103/PhysRevB.93.115316. URL <http://link.aps.org/doi/10.1103/PhysRevB.93.115316>
- [6] I. C. Diallo, D. O. Demchenko, Native point defects in GaN : A hybrid-functional study, *Phys. Rev. Applied* 6 (2016) 064002. doi:10.1103/PhysRevApplied.6.064002. URL <http://link.aps.org/doi/10.1103/PhysRevApplied.6.064002>
- [7] Y. Kumagai, L. A. Burton, A. Walsh, F. Oba, Electronic structure and defect physics of tin sulfides: SnS , Sn_2S_3 , and SnS_2 , *Phys. Rev. Applied* 6 (2016) 014009. doi:10.1103/PhysRevApplied.6.014009. URL <http://link.aps.org/doi/10.1103/PhysRevApplied.6.014009>

- [8] S. R. Lee, A. F. Wright, N. A. Modine, C. C. Battaile, S. M. Foiles, J. C. Thomas, A. Van der Ven, First-principles survey of the structure, formation energies, and transition levels of as-interstitial defects in indium arsenide, *Phys. Rev. B* 92 (2015) 045205. doi:10.1103/PhysRevB.92.045205. URL <http://link.aps.org/doi/10.1103/PhysRevB.92.045205>
- [9] V. Wang, Y. Kawazoe, W. T. Geng, Native point defects in few-layer phosphorene, *Phys. Rev. B* 91 (2015) 045433. doi:10.1103/PhysRevB.91.045433. URL <http://link.aps.org/doi/10.1103/PhysRevB.91.045433>
- [10] W. Sun, H. Ehteshami, P. A. Korzhavyi, Structure and energy of point defects in titanium nitride: An *ab initio* study, *Phys. Rev. B* 91 (2015) 134111. doi:10.1103/PhysRevB.91.134111. URL <http://link.aps.org/doi/10.1103/PhysRevB.91.134111>
- [11] D. Steiauf, J. L. Lyons, A. Janotti, C. G. V. de Walle, First-principles study of vacancy-assisted impurity diffusion in zinc oxide, *APL Materials* 2 (9) (2014) 096101. arXiv:<http://dx.doi.org/10.1063/1.4894195>, doi:10.1063/1.4894195. URL <http://dx.doi.org/10.1063/1.4894195>
- [12] C. G. V. de Walle, J. Neugebauer, First-principles calculations for defects and impurities: Applications to indium nitride, *Journal of Applied Physics* 95 (8) (2004) 3851–3879. arXiv:<http://dx.doi.org/10.1063/1.1682673>, doi:10.1063/1.1682673. URL <http://dx.doi.org/10.1063/1.1682673>
- [13] F. de Brito Mota, S. Azevedo, C. M. de Castilho, Structural and electronic properties of perfect and defective boron nitride nanoribbons: A dft study, *Physica E: Low-dimensional Systems and Nanostructures* 74 (2015) 233 – 240. doi:<http://dx.doi.org/10.1016/j.physe.2015.06.028>. URL <http://www.sciencedirect.com/science/article/pii/S1386947715301004>
- [14] W. Chen, Y. Li, G. Yu, Z. Zhou, Z. Chen, Electronic structure and reactivity of boron nitride nanoribbons with stone-wales defects, *Journal of Chemical Theory and Computation* 5 (11) (2009) 3088–3095, PMID: 26609988. arXiv:<http://dx.doi.org/10.1021/ct900388x>, doi:10.1021/ct900388x. URL <http://dx.doi.org/10.1021/ct900388x>

- [15] A. Manjanath, A. K. Singh, Low formation energy and kinetic barrier of stonewales defect in infinite and finite silicene, *Chemical Physics Letters* 592 (2014) 52 – 55. doi:<https://doi.org/10.1016/j.cplett.2013.12.010>.
URL <http://www.sciencedirect.com/science/article/pii/S0009261413014905>
- [16] S. Ögüt, J. R. Chelikowsky, Charge state dependent jahn-teller distortions of the *e*-center defect in crystalline si, *Phys. Rev. Lett.* 91 (2003) 235503. doi:[10.1103/PhysRevLett.91.235503](https://doi.org/10.1103/PhysRevLett.91.235503).
URL <https://link.aps.org/doi/10.1103/PhysRevLett.91.235503>
- [17] M. L. Tiago, J. R. Chelikowsky, Optical excitations in organic molecules, clusters, and defects studied by first-principles green’s function methods, *Phys. Rev. B* 73 (2006) 205334. doi:[10.1103/PhysRevB.73.205334](https://doi.org/10.1103/PhysRevB.73.205334).
URL <https://link.aps.org/doi/10.1103/PhysRevB.73.205334>
- [18] J. Kim, J. W. Wilkins, F. S. Khan, A. Canning, Extended si —p[311—p] defects, *Phys. Rev. B* 55 (1997) 16186–16197. doi:[10.1103/PhysRevB.55.16186](https://doi.org/10.1103/PhysRevB.55.16186).
URL <https://link.aps.org/doi/10.1103/PhysRevB.55.16186>
- [19] H.-P. Komsa, S. Kurasch, O. Lehtinen, U. Kaiser, A. V. Krasheninnikov, From point to extended defects in two-dimensional mos₂: Evolution of atomic structure under electron irradiation, *Phys. Rev. B* 88 (2013) 035301. doi:[10.1103/PhysRevB.88.035301](https://doi.org/10.1103/PhysRevB.88.035301).
URL <http://link.aps.org/doi/10.1103/PhysRevB.88.035301>
- [20] D. Le, T. B. Rawal, T. S. Rahman, Single-layer mos₂ with sulfur vacancies: Structure and catalytic application, *The Journal of Physical Chemistry C* 118 (10) (2014) 5346–5351. arXiv:<http://dx.doi.org/10.1021/jp411256g>, doi:[10.1021/jp411256g](https://doi.org/10.1021/jp411256g).
URL <http://dx.doi.org/10.1021/jp411256g>
- [21] H. L. Tuller, S. R. Bishop, Point defects in oxides: Tailoring materials through defect engineering, *Annual Review of Materials Research* 41 (1) (2011) 369–398. arXiv:<http://dx.doi.org/10.1146/annurev-matsci-062910-100442>, doi:[10.1146/annurev-matsci-062910-100442](https://doi.org/10.1146/annurev-matsci-062910-100442).
URL <http://dx.doi.org/10.1146/annurev-matsci-062910-100442>
- [22] L. Hu, T. Zhu, X. Liu, X. Zhao, Point defect engineering of high-performance bismuth-telluride-based thermoelectric materials, *Advanced Functional Materials* 24 (33) (2014) 5211–5218.

doi:10.1002/adfm.201400474.

URL <http://dx.doi.org/10.1002/adfm.201400474>

- [23] M. K. Nowotny, L. R. Sheppard, T. Bak, J. Nowotny, Defect chemistry of titanium dioxide. application of defect engineering in processing of tio2-based photocatalysts, *The Journal of Physical Chemistry C* 112 (14) (2008) 5275–5300. arXiv:<http://dx.doi.org/10.1021/jp077275m>, doi:10.1021/jp077275m.
URL <http://dx.doi.org/10.1021/jp077275m>
- [24] A. K. Singh, E. S. Penev, B. I. Yakobson, Vacancy clusters in graphane as quantum dots, *ACS Nano* 4 (6) (2010) 3510–3514. arXiv:<http://dx.doi.org/10.1021/nn1006072>, doi:10.1021/nn1006072.
URL <http://dx.doi.org/10.1021/nn1006072>
- [25] S. Bhowmick, U. V. Waghmare, Anisotropy of the stone-wales defect and warping of graphene nanoribbons: A first-principles analysis, *Phys. Rev. B* 81 (2010) 155416. doi:10.1103/PhysRevB.81.155416.
URL <https://link.aps.org/doi/10.1103/PhysRevB.81.155416>
- [26] C. Freysoldt, J. Neugebauer, C. G. Van de Walle, Fully *Ab Initio* finite-size corrections for charged-defect supercell calculations, *Phys. Rev. Lett.* 102 (2009) 016402. doi:10.1103/PhysRevLett.102.016402.
URL <http://link.aps.org/doi/10.1103/PhysRevLett.102.016402>
- [27] H.-P. Komsa, T. T. Rantala, A. Pasquarello, Finite-size supercell correction schemes for charged defect calculations, *Phys. Rev. B* 86 (2012) 045112. doi:10.1103/PhysRevB.86.045112.
URL <http://link.aps.org/doi/10.1103/PhysRevB.86.045112>
- [28] Y. Kumagai, F. Oba, Electrostatics-based finite-size corrections for first-principles point defect calculations, *Phys. Rev. B* 89 (2014) 195205. doi:10.1103/PhysRevB.89.195205.
URL <http://link.aps.org/doi/10.1103/PhysRevB.89.195205>
- [29] I. Dabo, B. Kozinsky, N. E. Singh-Miller, N. Marzari, Electrostatics in periodic boundary conditions and real-space corrections, *Phys. Rev. B* 77 (2008) 115139. doi:10.1103/PhysRevB.77.115139.
URL <http://link.aps.org/doi/10.1103/PhysRevB.77.115139>

- [30] M. Leslie, N. J. Gillan, The energy and elastic dipole tensor of defects in ionic crystals calculated by the supercell method, *Journal of Physics C: Solid State Physics* 18 (5) (1985) 973.
URL <http://stacks.iop.org/0022-3719/18/i=5/a=005>
- [31] N. D. M. Hine, K. Frensch, W. M. C. Foulkes, M. W. Finnis, Supercell size scaling of density functional theory formation energies of charged defects, *Phys. Rev. B* 79 (2009) 024112. doi:10.1103/PhysRevB.79.024112.
URL <http://link.aps.org/doi/10.1103/PhysRevB.79.024112>
- [32] W. Chen, A. Pasquarello, First-principles determination of defect energy levels through hybrid density functionals and gw, *Journal of Physics: Condensed Matter* 27 (13) (2015) 133202.
URL <http://stacks.iop.org/0953-8984/27/i=13/a=133202>
- [33] W. Chen, A. Pasquarello, Correspondence of defect energy levels in hybrid density functional theory and many-body perturbation theory, *Phys. Rev. B* 88 (2013) 115104. doi:10.1103/PhysRevB.88.115104.
URL <http://link.aps.org/doi/10.1103/PhysRevB.88.115104>
- [34] G. Makov, M. C. Payne, Periodic boundary conditions in *ab initio* calculations, *Phys. Rev. B* 51 (1995) 4014–4022. doi:10.1103/PhysRevB.51.4014.
URL <http://link.aps.org/doi/10.1103/PhysRevB.51.4014>
- [35] S. Lany, A. Zunger, Assessment of correction methods for the band-gap problem and for finite-size effects in supercell defect calculations: Case studies for zno and gaas, *Phys. Rev. B* 78 (2008) 235104. doi:10.1103/PhysRevB.78.235104.
URL <http://link.aps.org/doi/10.1103/PhysRevB.78.235104>
- [36] D. Wang, D. Han, X.-B. Li, S.-Y. Xie, N.-K. Chen, W. Q. Tian, D. West, H.-B. Sun, S. B. Zhang, Determination of formation and ionization energies of charged defects in two-dimensional materials, *Phys. Rev. Lett.* 114 (2015) 196801. doi:10.1103/PhysRevLett.114.196801.
URL <http://link.aps.org/doi/10.1103/PhysRevLett.114.196801>
- [37] T.-L. Chan, A. J. Lee, J. R. Chelikowsky, An effective capacitance model for computing the electronic properties of charged defects in crystals, *Computer Physics Communications* 185 (6) (2014) 1564 –

1569. doi:<https://doi.org/10.1016/j.cpc.2014.02.020>.
URL <http://www.sciencedirect.com/science/article/pii/S0010465514000642>
- [38] H.-P. Komsa, A. Pasquarello, Finite-size supercell correction for charged defects at surfaces and interfaces, *Phys. Rev. Lett.* 110 (2013) 095505. doi:10.1103/PhysRevLett.110.095505.
URL <http://link.aps.org/doi/10.1103/PhysRevLett.110.095505>
- [39] J.-Y. Noh, H. Kim, Y.-S. Kim, Stability and electronic structures of native defects in single-layer mos_2 , *Phys. Rev. B* 89 (2014) 205417. doi:10.1103/PhysRevB.89.205417.
URL <http://link.aps.org/doi/10.1103/PhysRevB.89.205417>
- [40] H.-P. Komsa, N. Berseneva, A. V. Krasheninnikov, R. M. Nieminen, Charged point defects in the flatland: Accurate formation energy calculations in two-dimensional materials, *Phys. Rev. X* 4 (2014) 031044. doi:10.1103/PhysRevX.4.031044.
URL <http://link.aps.org/doi/10.1103/PhysRevX.4.031044>
- [41] H.-P. Komsa, A. V. Krasheninnikov, Native defects in bulk and monolayer mos_2 from first principles, *Phys. Rev. B* 91 (2015) 125304. doi:10.1103/PhysRevB.91.125304.
URL <http://link.aps.org/doi/10.1103/PhysRevB.91.125304>
- [42] S. Kim, K. J. Chang, J.-S. Park, Finite-size supercell correction scheme for charged defects in one-dimensional systems, *Phys. Rev. B* 90 (2014) 085435. doi:10.1103/PhysRevB.90.085435.
URL <http://link.aps.org/doi/10.1103/PhysRevB.90.085435>
- [43] D. Vinichenko, M. Gokhan Sensoy, C. M. Friend, E. Kaxiras, Accurate formation energies of charged defects in solids: a systematic approach, *ArXiv e-prints* arXiv:1701.02521.
- [44] M. G. Sensoy, D. Vinichenko, W. Chen, C. M. Friend, E. Kaxiras, Strain effects on the behavior of isolated and paired sulfur vacancy defects in monolayer mos_2 , *Phys. Rev. B* 95 (2017) 014106. doi:10.1103/PhysRevB.95.014106.
URL <https://link.aps.org/doi/10.1103/PhysRevB.95.014106>

- [45] D. Broberg, B. Medasani, N. Zimmermann, A. Canning, M. Haranczyk, M. Asta, G. Hautier, PyCDT: A Python toolkit for modeling point defects in semiconductors and insulators, ArXiv e-prints arXiv:1611.07481.
- [46] E. Pan, J. Vidal, S. Jobic, C. Latouche, Presentation of the pydef post-treatment python software to compute publishable charts for defect energy formation, Chemical Physics Letters 671 (Supplement C) (2017) 124 – 130. doi:<https://doi.org/10.1016/j.cplett.2017.01.001>. URL <http://www.sciencedirect.com/science/article/pii/S0009261417300015>
- [47] G. Rossum, Python reference manual, Tech. rep., Amsterdam, The Netherlands, The Netherlands (1995).
- [48] S. Behnel, R. Bradshaw, C. Citro, L. Dalcin, D. Seljebotn, K. Smith, Cython: The best of both worlds, Computing in Science Engineering 13 (2) (2011) 31 –39. doi:10.1109/MCSE.2010.118.
- [49] X. Gonze, C. Lee, Dynamical matrices, born effective charges, dielectric permittivity tensors, and interatomic force constants from density-functional perturbation theory, Phys. Rev. B 55 (1997) 10355–10368. doi:10.1103/PhysRevB.55.10355. URL <http://link.aps.org/doi/10.1103/PhysRevB.55.10355>
- [50] S. Baroni, S. de Gironcoli, A. Dal Corso, P. Giannozzi, Phonons and related crystal properties from density-functional perturbation theory, Rev. Mod. Phys. 73 (2001) 515–562. doi:10.1103/RevModPhys.73.515. URL <http://link.aps.org/doi/10.1103/RevModPhys.73.515>
- [51] P. Giannozzi, S. Baroni, N. Bonini, M. Calandra, R. Car, C. Cavazzoni, D. Ceresoli, G. L. Chiarotti, M. Cococcioni, I. Dabo, A. D. Corso, S. de Gironcoli, S. Fabris, G. Fratesi, R. Gebauer, U. Gerstmann, C. Gougoussis, A. Kokalj, M. Lazzeri, L. Martin-Samos, N. Marzari, F. Mauri, R. Mazzarello, S. Paolini, A. Pasquarello, L. Paulatto, C. Sbraccia, S. Scandolo, G. Sclauzero, A. P. Seitsonen, A. Smogunov, P. Umari, R. M. Wentzcovitch, Quantum espresso: a modular and open-source software project for quantum simulations of materials, Journal of Physics: Condensed Matter 21 (39) (2009) 395502.
- [52] J. P. Perdew, A. tunger, Self-interaction correction to density-functional approximations for many-electron systems, Phys. Rev. B 23 (1981) 5048–5079. doi:10.1103/PhysRevB.23.5048.

- [53] P. E. Blöchl, Projector augmented-wave method, *Phys. Rev. B* 50 (1994) 17953–17979. doi:10.1103/PhysRevB.50.17953.
URL <http://link.aps.org/doi/10.1103/PhysRevB.50.17953>
- [54] J. P. Perdew, M. Ernzerhof, K. Burke, Rationale for mixing exact exchange with density functional approximations, *The Journal of Chemical Physics* 105 (22) (1996) 9982–9985. doi:<http://dx.doi.org/10.1063/1.472933>.
- [55] L. Dalcín, R. Paz, M. Storti, Mpi for python, *J. Parallel Distrib. Comput.* 65 (9) (2005) 1108–1115. doi:10.1016/j.jpdc.2005.03.010.
URL <http://dx.doi.org/10.1016/j.jpdc.2005.03.010>